

Anisotropic transport properties of quasiballistic InAs nanowires under high magnetic field

Florian Vigneau,¹ Zaiping Zeng,² Walter Escoffier,¹ Philippe Caroff,^{3,4} Renaud Leturcq,^{3,5}
Yann-Michel Niquet,² Bertrand Raquet,¹ and Michel Goiran¹

¹LNCMI, Université de Toulouse, CNRS, INSA, UPS, Toulouse, France

²Université Grenoble Alpes, CEA, INAC-MEM, L_Sim, F-38000 Grenoble, France

³Institute of Electronics Microelectronics and Nanotechnology, CNRS-UMR 8520, ISEN Department, Avenue Poincaré,
CS 60069, 59652 Villeneuve d'Ascq Cedex, France

⁴Department of Electronic Materials Engineering, Research School of Physics and Engineering,
The Australian National University, Canberra, Australian Capital Territory 0200, Australia

⁵Materials Research and Technology (MRT) Department, Luxembourg Institute of Science and Technology (LIST),
5, avenue des Hauts-Fourneaux, L-4362 Esch-sur-Alzette, Luxembourg



(Received 5 November 2017; published 27 March 2018)

The magnetoconductance of a long channel InAs nanowire based field effect transistor in the quasiballistic regime under large magnetic field is investigated. The quasi-1D nanowire is fully characterized by a bias voltage spectroscopy and measurements under magnetic field up to 50 T applied either perpendicular or parallel to the nanowire axis lifting the spin and orbital degeneracies of the subbands. Under normal magnetic field, the conductance shows quantized steps due to the backscattering reduction and a decrease due to depopulation of the 1D modes. Under axial magnetic field, a quasiscillatory behavior is evidenced due to the coupling of the magnetic field with the angular momentum of the wave function. In addition the formation of cyclotron orbits is highlighted under high magnetic field. The experimental results are compared with theoretical calculation of the 1D band structure and related parameters.

DOI: [10.1103/PhysRevB.97.125308](https://doi.org/10.1103/PhysRevB.97.125308)

I. INTRODUCTION

Narrow band-gap III-V based nanowires (NWs) synthesized in a bottom up approach are subject to intense research thanks to their exceptional mobility that encourages their integration on silicon substrates in order to extend the limit of Moore law [1–3]. Moreover, InAs NWs have been identified as a platform for the realization of topological Majorana fermion states [4–8], due to strong spin orbit coupling, high g^* factor of the bulk material [9] and ability to host superconductivity by proximity effect [10–13]. The confinement of the electron gas inside a 1D conductor down to the nanometer scale alters the electronic band structure, resulting in a set of quasiparabolic degenerate electric subbands. The investigation of the subband occupation as a function of the carrier density or the magnetic field is critical but complicated by the narrow band gap of InAs that prevents any optical investigation.

Several groups have recently investigated low temperature transport measurements in the ballistic and quasiballistic regimes [11, 14–20]. The quasiballistic regime is reached when the mean free path ℓ is of the order of the channel length L . The carriers have then a certain probability to be transmitted without being backscattered, characterized by a transmission coefficient $Tr = \ell/(\ell + L)$ [21]. The conductance of a one-dimensional system is quantized in units of $Tr \cdot e^2/h$ (with e the elementary charge and h the Planck constant) for each occupied subband, allowing us to probe the subbands structure. Conductance quantization in InAs NWs has been observed by A. Javey *et al.* [14, 15] and magnetotransport experiments under

axial magnetic field have been performed by Holloway *et al.* to study how the band bends at the surface of the NW [18]. Recently, we have reported the band structure evolution under normal magnetic field (B perpendicular to the NW axis) [16] from tight-binding simulations and magnetotransport experiments.

In this paper, we investigate the magnetoconductance of an individual InAs NW under magnetic field, up to 50 T, oriented perpendicular or parallel to the NW axis. The energy spectrum is first characterized by a bias voltage spectroscopy at $B = 0$ T. In a second part we investigate magnetotransport with magnetic field set perpendicular to the NW axis (normal configuration). The high magnetic field induces a magnetic depopulation of the subband as well as an increase of transmission due to the formation of cyclotronic orbits. In a third part, the electronic transport with the field set parallel to the NW axis (axial configuration) is presented together with band structure simulations. The magnetic field evolution of the quasi-1D energy spectrum enables us to interpret qualitatively and quantitatively the experimental data.

The NWs of diameter $d = 50 \pm 5$ nm are synthesized by gold-assisted gas-source molecular beam epitaxy on InP(111)B substrates and exhibit a pure wurtzite crystal structure [22, 23]. After the growth, they are deposited on a degenerately n -doped Si substrate with a 225 nm thick SiO₂ insulating layer at the surface. This substrate acts as a back gate [Fig. 1(c)]. Two Ti/Au (10/150 nm) contacts, distant by $L = 2 \mu\text{m}$, are patterned along the NW by electron beam lithography. The conductance is measured using standard lock-in techniques with an ac bias voltage around 2 mV_{rms},

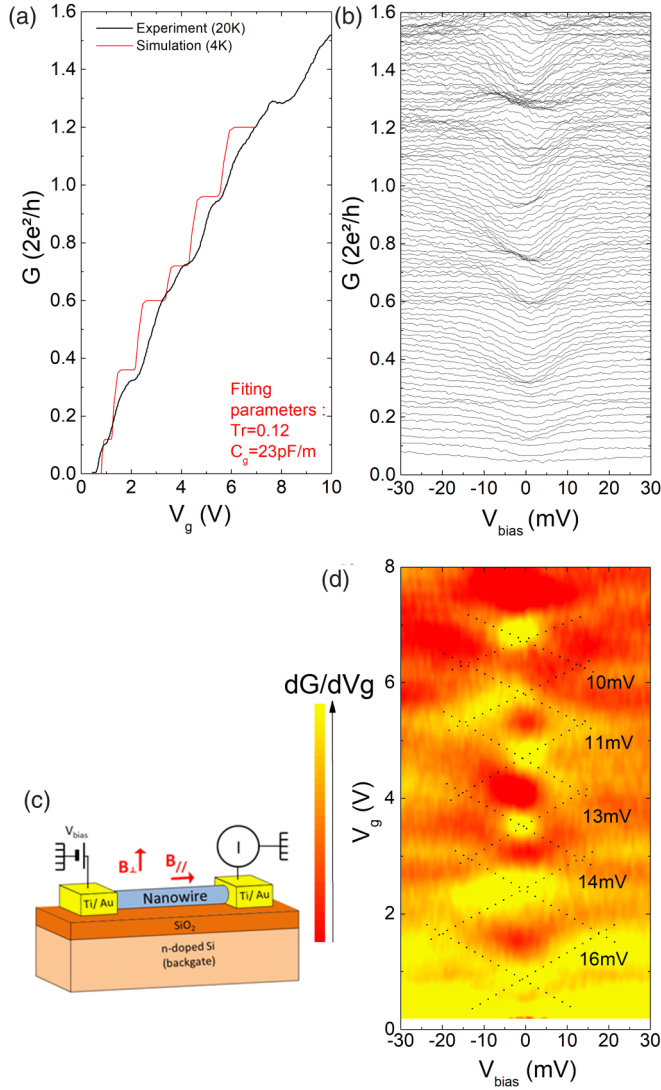


FIG. 1. (a) Experimental conductance versus gate voltage superimposed with conductance simulation (see text), extracted at a bias voltage of 2 mV_{rms}. (b) Conductance versus bias voltage measured at 20 K with V_g from 0.2 V to 12 V with steps of 0.1 V. (c) Sketch of the device. (d) Transconductance $\partial G/\partial V_g$ derived from (b). The dashed lines are just guides to the eye to help follow the main maxima evolution. The bias energy at the transconductance maxima crossing is given in the figure.

in a frequency range of [1–4] kHz, under pulsed magnetic field (total duration 0.3 s) up to 50 T. For the bias voltage spectroscopy, the dc bias is swept (0–30 mV), while an ac voltage (0.5 mV_{rms}, 23 Hz) is superimposed. The measurement was performed at a temperature of 20 K to avoid universal conductance fluctuations. A 3 k Ω series resistance, attributed to the contact, has been subtracted from the original data (justified in Sec. III).

II. BIAS VOLTAGE SPECTROSCOPY

In Fig. 1, the transfer characteristics and the results of the bias spectroscopy are described. Plateaus are visible on the conductance versus gate voltage $G(V_g)$ characteristics

[Fig. 1(a)], corresponding to the conductance quantization, and highlighted by dense areas in the bias voltage spectroscopy in Fig. 1(b) [24]. The transconductance $\frac{\partial G}{\partial V_g}$ maxima in Fig. 1(d) shows the typical diamond shape structure observed in 1D systems [17,24,25]. The subband energy spacing $\Delta E = E_{n+1} - E_n$ is extracted from the bias voltage ΔV_{bias} at maxima crossing with $e\Delta V_{\text{bias}} = \Delta E$ [24].

The experimental conductance is fitted with the Landauer-Büttiker formula:

$$G(E_F) = \frac{e^2}{h} \sum_n f(E_n, E_F, T) \cdot Tr, \quad (1)$$

where E_n is the energy of the n th 1D subband, obtained previously by the bias voltage spectroscopy, and $f(E_n, E_F, T) = 1/(1 + \exp(\frac{E_n - E_F}{k_B T}))$ is the Fermi distribution at the subband edge (k_B is the Boltzmann constant). The relation between the gate voltage and Fermi energy E_F is given by:

$$V_g(E_F) = \frac{eN_e(E_F)}{C_g L}. \quad (2)$$

$N_e(E_F) = \int \sum_n \rho_n(E) f(E_n, E_F, T) dE$ is the carrier density, and $\rho_n(E) = \frac{L\sqrt{2m^*}}{h\sqrt{E - E_n}}$ is the density of states calculated with the bulk InAs effective mass $m^* = 0.023 m_0$ [Fig. 1(a)]. The combination of equation (1) and (2) allows us to calculate the conductance versus gate voltage. The transmission coefficient $Tr = \ell/(\ell + L)$ and the linear gate coupling C_g are set as fitting parameters [16]. Orbital and spin degeneracies are introduced consistently with the band structure simulation presented in part IV. A good agreement is found for $C_g = 23$ pF/m and $Tr = 0.12$ for all subbands, which gives a mean free path $\ell \approx 280$ nm consistent with a quasiballistic regime, and in the range of the recent values reported for this system [14,17]. The obtained linear gate coupling is much smaller than the geometrical capacitance between an infinite cylinder and a plane $C_{\text{geo}} = 64$ pF/m, as frequently observed in similar systems [15,16,26–28]. This is mainly attributed to finite size effects and electrostatic screening of the contacts. Including nonparabolicity corrections in the density of states does not significantly change C_g and Tr .

III. NORMAL MAGNETIC FIELD

Between the measurement presented in the first part and the one presented in this section, the device was exposed to ambient atmosphere, but we want to stress that the principal characteristics remain preserved. The conductance is measured under pulsed magnetic field, perpendicular to the nanowire axis, for different values of the gate voltage [Fig. 2(b)]. The transconductance $\frac{\partial G}{\partial V_g}$ versus B and V_g was computed from the experimental results [Fig. 2(c)] to give an indirect view of the evolution of the subbands.

The magnetoconductance [Fig. 2(b)] mainly decreases with increasing magnetic field due to the magnetic depopulation of the subbands [29]. Indeed, the normal magnetic field induces a diamagnetic shift that moves the subbands energy upward. Simultaneously it flattens the dispersion relation at the bottom of the subbands [16], increasing the density of states. More carriers are then required to raise the Fermi energy. This explains why only two plateaus are visible in the interpolated

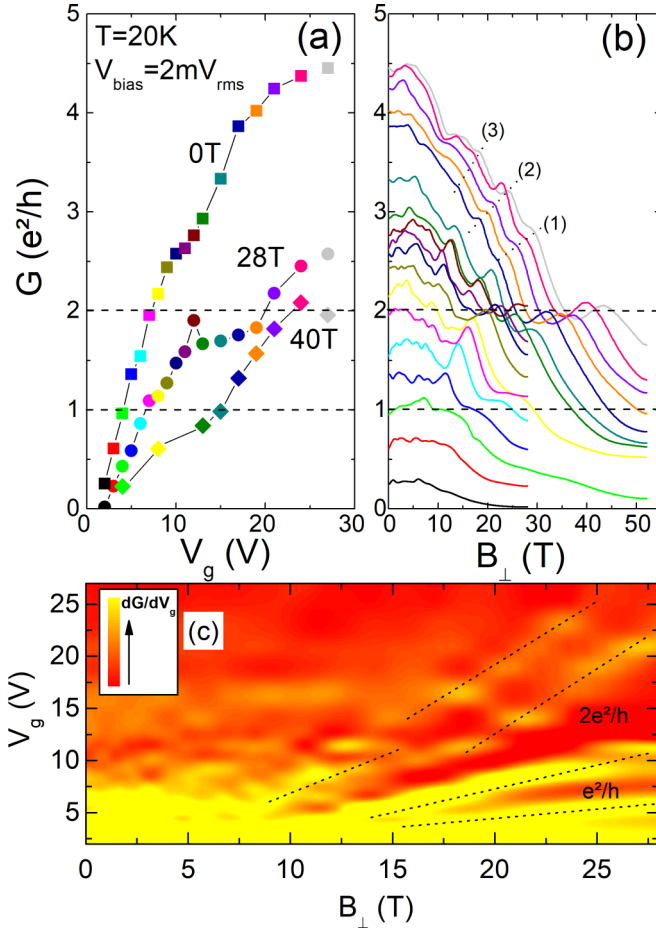


FIG. 2. (a) Transfer characteristic of the device at 0 T, 28 T, and 40 T interpolated from the magnetoconductance curves in (b) reported by points of the same color. (b) Magnetoconductance curves for a range of gate voltage from 2 V to 27 V. (c) Transconductance $\partial G/\partial V_g$ derived from the data in (b). The dashed lines are just guides to the eye to help follow the main maxima evolution.

transfer characteristic at 28 T and 40 T [Fig. 2(a)] while up to around 10 subbands are occupied at 0 T for $V_g = [0-20]$ V. For the same reason, the transconductance maxima in Fig. 2(c) move to higher V_g with increasing magnetic field.

The transconductance maxima of the two lowest subbands are particularly visible above 10 T [Fig. 2(c)]. They split around 15 T as the Zeeman energy, for $g^* = 7$ [17,30], exceeds the thermal broadening, $g^* \mu_B B \approx 3.5 k_B T \approx 6$ meV (with μ_B the Bohr magneton).

Below 10 T, the magnetoconductance exhibits broadened conductance fluctuations. Considering the high number of occupied subbands at zero magnetic field, the direct relation between these fluctuations and the band structure is difficult to establish.

From 10 T to 20 T, conductance plateaus are more visible. The conductance spacing between the plateaus labeled (1), (2), and (3) [Fig. 2(b)] becomes larger with increasing magnetic field, suggesting an enhancement of transmission. Under high magnetic field, the carriers precess on cyclotron orbits smaller than the NW diameter. In normal configuration, quasi-1D systems tend toward a two-dimensional electron gas (2DEG)

in the quantum Hall effect regime [31–33]. The current is then carried by edge states with a reduced backscattering.

Above 20 T the transmission of the two lowest conductance plateaus stops increasing with magnetic field suggesting that the ballistic regime is reached. The transmission is then equal to 1 despite the long channel length of the device. A 3 k Ω contact resistance is subtracted in order to set the conductance plateaus at e^2/h and $2e^2/h$. Further investigation of this effect could be performed by successfully contacting NWs in a Hall bar geometry.

For magnetic field higher than 30 T, the e^2/h plateau disappears and the conductance decreases monotonously. We attribute these effects to the depletion of the wire by the magnetic field. Diamagnetism indeed raises the subbands of the nanowire with respect to the Fermi energy in the contacts when increasing magnetic field. This results in an increase of the threshold voltage, or equivalently into a decrease of the carrier density (which flow back to the contacts) for a given gate voltage. When the Fermi energy reaches the bottom of the first subband, the channel gets completely emptied, all subbands being ultimately raised above the chemical potential.

IV. AXIAL MAGNETIC FIELD

The band structure of a 50 nm diameter InAs NW under magnetic field applied parallel to the NW axis is calculated using a $sp^3d^5s^*$ tight-binding model [34,35]. The result is plotted in Fig. 3. The subband spacings at 0 T are in the same range as the one extracted experimentally by the bias voltage spectroscopy. Unlike the normal configuration, the subbands dispersion along the NW axis experiences little changes, however the subband energy is affected in a complex manner. In a simple effective mass picture, each subband is characterized by two quantum numbers: n for the radial part and l for the angular part. For a given value of n and for $l \neq 0$, the $[n, +l]$ and $[n, -l]$ subbands are degenerate at $B = 0$ T. The angular momentum couples with magnetic field lifting the orbital degeneracy at finite B [18]. The energy of the subbands with positive (negative) angular momentum is shifted to high (low) energy as the field increases. This generates a complex subband crossing pattern represented in Fig. 3(a). Under high magnetic field, diamagnetism shifts the whole subband energy spectrum upward. At very large magnetic field, the subbands merge together into Landau levels. The Zeeman effect splits the spin level, but stays relatively weak compared to the orbital degeneracy lifting.

The conductance and the Fermi energy versus magnetic field in the ballistic regime are calculated according to the Landauer-Bütticker formalism in Fig. 3(b) by summing the contributions from all electronic states at a given B :

$$G = \frac{1}{V_{\text{bias}}} \left(\frac{e}{L} \sum_{k>0,n} v_{n,k} f(E_{n,k}, E_F^+, T) \right) - \frac{1}{V_{\text{bias}}} \left(\frac{e}{L} \sum_{k<0,n} v_{n,k} f(E_{n,k}, E_F^-, T) \right). \quad (3)$$

E_F^\pm stand for the quasi Fermi energy at the two terminals $E_F^+ - E_F^- = eV_{\text{bias}}$, $E_{n,k}$ is the energy of each state, and $v_{n,k} = (1/\hbar)(\partial E_{n,k}/\partial k)$ its velocity. Taking into account the

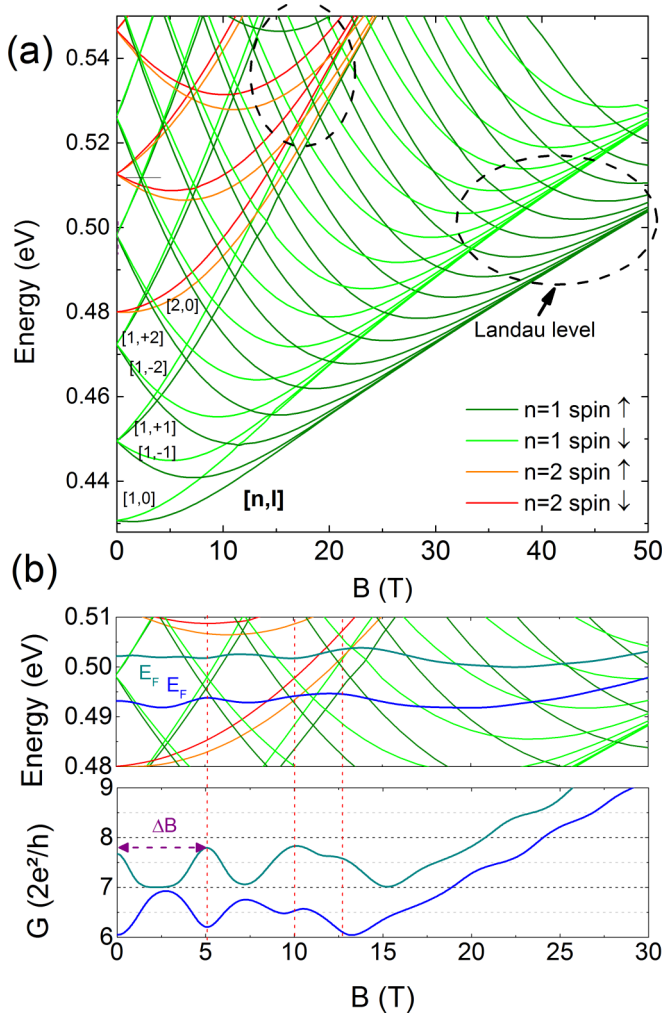


FIG. 3. (a) Simulation of the evolution of the $k = 0$ subbands energy for a 50 nm diameter InAs NW versus axial magnetic field. The subbands merge into Landau levels at high magnetic field. (b) Theoretical conductance in ballistic regime, $T = 20$ K and $V_{\text{bias}} = 2$ V m, versus axial magnetic field for two density of carriers (bottom) and corresponding Fermi energy in the band structure simulation (top). The two conductance curves move toward and away consecutively around a symmetry axis at $7 G_0$ with quasiperiod ΔB .

temperature $T = 20$ K and a bias voltage of $V_{\text{bias}} = 2$ mV rounds the conductance plateaus.

At relatively low magnetic field ($B \leq 20$ T), the magnetoconductance evolution shares similarities with tubular systems, as is the case for strong band bending at the surface of the NW [18,36] or core-shell structures [37,38]. For two carriers densities with an initial Fermi energy (at $B = 0$ T) separated by one degenerate subband, we notice a few fingerprints that will be useful to understand the experimental results. (1) The magnetoconductance evolves quasiperiodically due to the successive population and depopulation of the subbands, with a quasiperiod $\Delta B \approx 5$ T. (2) The magnetoconductance curves are quasymmetric around the mean conductance value axis. This defines “convergence” (“divergence”) areas where the curves move towards (away) from each other consecutively.

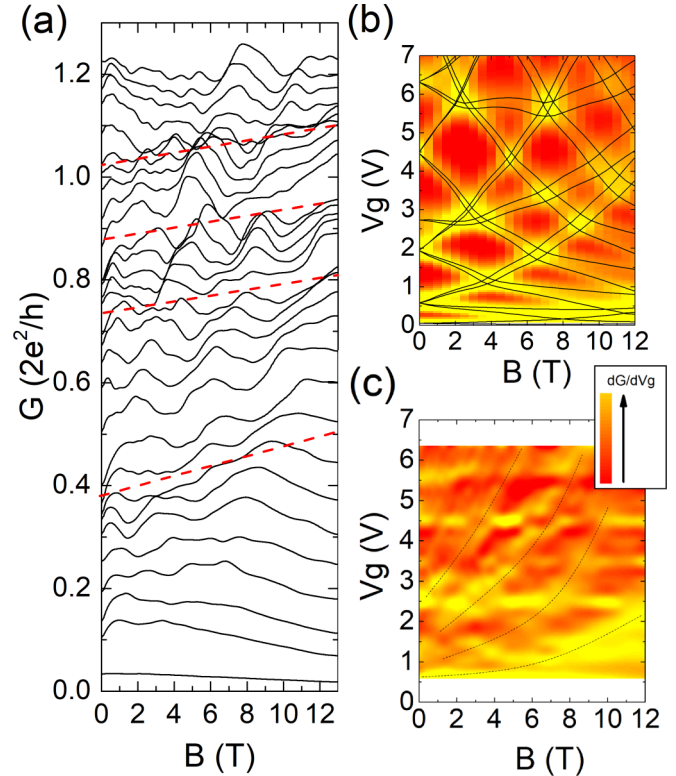


FIG. 4. (a) Magnetoconductance measurements in axial configuration up to 13 T for a range of gate voltage from 0.6 V to 6.4 V with steps of 0.2 V. The symmetric axis around which the quasiperiodic magnetoconductance curves move toward and away consecutively are marked by red dashed lines. (b) Theoretical transconductance $\frac{\partial G}{\partial V_g}$ obtained from band structure simulation. The black lines are the coordinates where the Fermi energy is aligned with the bottom of each subband. (c) Experimental transconductance derived from (a). The dashed lines are just guides to the eye to help follow the main maxima evolution.

(3) The divergence areas coincide with crossing of subbands in Fig. 3(b), top panel.

In our simulation the wave functions of the carriers are not confined in a shell at the surface of the NW. The results show that the flux enclosed by the NW cross section in the quasiperiod $\pi(d/2)^2 \Delta B$ is not equal to the quantum of flux $\Phi_0 = e/h$. Moreover subbands with larger radial number ($n > 1$) are involved in the spectrum.

The magnetoconductance in axial configuration was measured in the same condition as for the normal configuration [Fig. 4(a)]. From 0 T to 13 T, the magnetoconductance exhibits qualitatively the same behavior as the simulation: (1) quasiperiodic modulation, (2) symmetry around particular axes (marked by the red lines), and (3) “divergence” areas. The amplitude of the quasis oscillations is of the order of $2e^2/h \cdot Tr$ corresponding to the conductance of one spin degenerate subband. The quasiperiod, of the order of $\Delta B = 3$ T $\equiv 1.42\Phi_0$, is distinct from one flux quantum enclosed by the NW cross section. ΔB is also smaller than the quasiperiod of the simulation. This discrepancy might be attributed to the fact that the electric field generated by the gate has not been taken into account for the simulation.

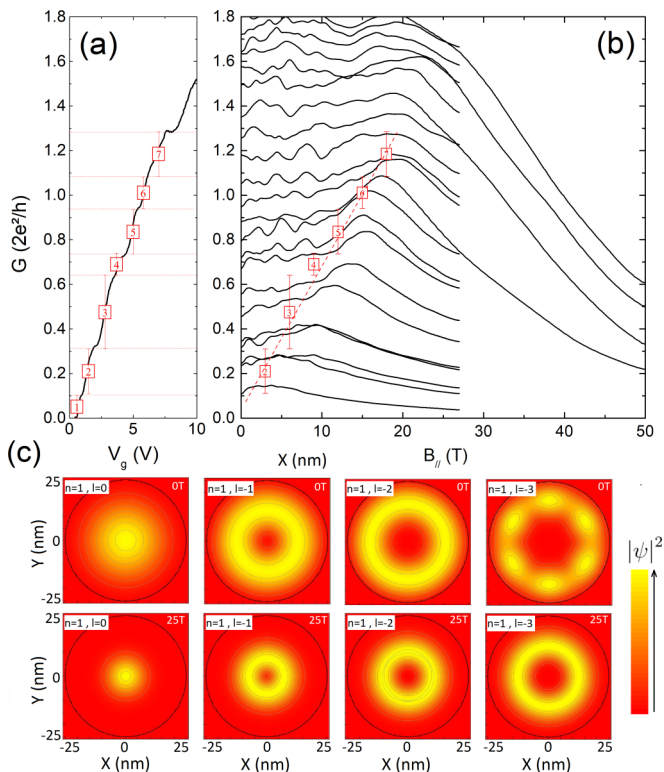


FIG. 5. (a) Transfer characteristic of the device. The red number letters represent the number N of occupied degenerate subbands at 0 T (placed at the average conductance value). (b) Magnetoconductance measurement for a set of gate voltages. The letters are placed at the same conductance as in (a) and at magnetic field $B_c = (N - 1)\Delta B$ in (b). (c) Cut in a plane perpendicular to the NW axis of the square modulus of the electronic wave function $|\psi|^2$ of the subbands $n = 1$ and $l = [0, -1, -2, -3]$, at 0 T and 25 T, issued from the band structure simulation. Note that the tight-binding wave functions can show a complex angular dependence for large l 's because the NW has, practically, only a threefold symmetry axis.

The transconductance $\frac{\partial G}{\partial V_g}$ is obtained by deriving the conductance versus gate voltage [Figs. 4(b) and 4(c)]. The one issued from the experimental results shows maxima, which allows following the band structure evolution with magnetic field. The diamond shape structure observed in the simulation is not clearly visible in the experimental results due to the broadening of the conductance plateaus. Nevertheless, the two figures share similarities, in particular the maxima that move upward with magnetic field.

Finally, under high magnetic field the simulated subbands merge into Landau levels [Fig. 3(a)]. The subbands $[1, l = 0]$ and $[1, l < 0]$ converge into the lowest Landau level while the subband $[1, l = 1]$, $[2, l = 0]$, and $[2, l < 0]$ form the second one. The carriers are distributed over cyclotron orbits in the plane perpendicular to the NW axis as illustrated by the

calculated wave functions [Fig. 5(c)]. At 25 T, the radial extent of the $n = 1, l = 0$ level is $\sqrt{\langle r^2 \rangle} = 7.5$ nm, while the radial extents of the $n = 1, l = -1, -2, -3$ levels are, respectively, $\sqrt{\langle r^2 \rangle} = 10.4, 12.6,$ and 14.4 nm. This fits the formula for the cyclotron radius of electronic states in 2DEG under normal magnetic field $r = (2(\tilde{n} + 1)\hbar/eB)^{1/2}$, \tilde{n} being the sublevel index. This illustrates the fact that the magnetic confinement overcomes the electronic confinement.

When the Fermi level ends up pinned in the nearly degenerate subbands that merge into the lowest lowest Landau level, the conductance stops oscillating and starts to decrease monotonously. On the contrary, the simulation, which assumes that the capacitance and carrier concentration are independent of B , shows an increase of conductance at high magnetic field [Fig. 3(b)]. This discrepancy results from a drop of the (quantum) capacitance and carrier concentration at high B , as observed previously for perpendicular magnetic field. Indeed, diamagnetism keeps raising the subbands of the nanowire with respect to the Fermi energy in the contacts, which progressively empties the nanowire. This may be accompanied by an increase of scattering within the highly degenerate subbands at the bottom of that Landau level. Ultimately, the nanowire gets completely depleted by the magnetic field, as the last subband crosses the Fermi energy. The Fermi level will cross $N - 1$ spin degenerate subbands before reaching the edge of the Landau level, with N the number of degenerate modes occupied at $B = 0$ T, which can be taken as the plateau index in Fig. 5(a). The corresponding magnetic field can thus be estimated at $B_c \simeq (N - 1)\Delta B$. This estimate fits nicely the beginning of the conductance drop in Fig. 5(b). This result highlights the formation of Landau levels perpendicular to the axis of the nanowire.

V. CONCLUSION

In conclusion, we have measured the magnetotransport properties of InAs NWs in the quasiballistic regime, with magnetic field up to 50 T. The magnetoconductance curves have shown a distinct behavior according to the direction of magnetic field. We have interpreted qualitatively and quantitatively the results in terms of spin and orbital dependent subband evolution in agreement with the band structure simulations. We have also evidenced the formation of Landau states and cyclotron orbits under high magnetic field in both configurations. These findings might be useful for the understanding of future magnetotransport experiments involving nanowires.

ACKNOWLEDGMENTS

High magnetic field measurements were performed at LNCMI under the EMFL proposal TSC10-213. Parts of the calculations were run on the CCRT/Curie machine using allocations from GENCI. This work is supported by the Grant NEXT N° ANR-10-LABX-0037 in the framework of the ‘‘Programme des Investissements d’Avenir’’.

[1] S. A. Dayeh, D. P. Aplin, X. Zhou, P. K. Yu, E. T. Yu, and D. Wang, *Small* **3**, 326 (2007).

[2] K. Tomioka, M. Yoshimura, and T. Fukui, *Nature (London)* **488**, 189 (2012).

- [3] H. Schmid, M. Borg, K. Moselund, L. Gignac, C. M. Breslin, J. Bruley, D. Cutaia, and H. Riel, *Appl. Phys. Lett.* **106**, 233101 (2015).
- [4] A. Y. Kitaev, *Phys.-Usp.* **44**, 131 (2001).
- [5] Y. Oreg, G. Refael, and F. von Oppen, *Phys. Rev. Lett.* **105**, 177002 (2010).
- [6] V. Mourik, K. Zuo, S. M. Frolov, S. R. Plissard, E. P. A. M. Bakkers, and L. P. Kouwenhoven, *Science* **336**, 1003 (2012).
- [7] A. Das, Y. Ronen, Y. Most, Y. Oreg, M. Heiblum, and H. Shtrikman, *Nat. Phys.* **8**, 887 (2012).
- [8] M. Deng, S. Vaitiekėnas, E. B. Hansen, J. Danon, M. Leijnse, K. Flensberg, J. Nygård, P. Krogstrup, and C. M. Marcus, *Science* **354**, 1557 (2016).
- [9] J. Konopka, *Phys. Lett. A* **26**, 29 (1967).
- [10] W. Chang, S. M. Albrecht, T. S. Jespersen, F. Kuemmeth, P. Krogstrup, J. Nygård, and C. M. Marcus, *Nat. Nano* **10**, 232 (2015).
- [11] S. Abay, D. Persson, H. Nilsson, H. Q. Xu, M. Fogelström, V. Shumeiko, and P. Delsing, *Nano Lett.* **13**, 3614 (2013).
- [12] E. M. Spanton, M. Deng, S. Vaitiekėnas, P. Krogstrup, J. Nygård, C. M. Marcus, and K. A. Moler, *Nat. Phys.* **13**, 1177 (2017).
- [13] F. K. de Vries, T. Timmerman, V. P. Ostroukh, J. van Veen, A. J. Beukman, F. Qu, M. Wimmer, B.-M. Nguyen, A. A. Kiselev, W. Yi *et al.*, [arXiv:1709.03727](https://arxiv.org/abs/1709.03727).
- [14] S. Chuang, Q. Gao, R. Kapadia, A. C. Ford, J. Guo, and A. Javey, *Nano Lett.* **13**, 555 (2013).
- [15] A. C. Ford, S. B. Kumar, R. Kapadia, J. Guo, and A. Javey, *Nano Lett.* **12**, 1340 (2012).
- [16] F. Vigneau, V. Prudkoviy, I. Duchemin, W. Escoffier, P. Caroff, Y.-M. Niquet, R. Leturcq, M. Goiran, and B. Raquet, *Phys. Rev. Lett.* **112**, 076801 (2014).
- [17] S. Heedt, W. Prost, J. Schubert, D. Grützmacher, and T. Schäpers, *Nano Lett.* **16**, 3116 (2016).
- [18] G. W. Holloway, D. Shiri, C. M. Haapamaki, K. Willick, G. Watson, R. R. LaPierre, and J. Baugh, *Phys. Rev. B* **91**, 045422 (2015).
- [19] J. Gooth, V. Schaller, S. Wirths, H. Schmid, M. Borg, N. Bologna, S. Karg, and H. Riel, *Appl. Phys. Lett.* **110**, 083105 (2017).
- [20] J. Gooth, M. Borg, H. Schmid, V. Schaller, S. Wirths, K. Moselund, M. Luisier, S. Karg, and H. Riel, *Nano Lett.* **17**, 2596 (2017).
- [21] S. Datta, *Electronic Transport in Mesoscopic Systems* (Cambridge University Press, Cambridge, UK, 1997).
- [22] C. Rolland, P. Caroff, C. Coinon, X. Wallart, and R. Leturcq, *Appl. Phys. Lett.* **102**, 223105 (2013).
- [23] C. Thelander, P. Caroff, S. Plissard, and K. A. Dick, *Appl. Phys. Lett.* **100**, 232105 (2012).
- [24] I. van Weperen, O. Gul, S. R. Plissard, E. P. A. M. Bakkers, S. M. Frolov, and L. P. Kouwenhoven, *Nano Lett.* **13**, 387 (2013).
- [25] L. I. Glazman and A. V. Khaetskii, *JETP Lett.* **48**, 591 (1988).
- [26] V. K. Andrey, P.-B. Ronit, M. Diana, and S. Hadas, *Nano Lett.* **10**, 3439 (2010).
- [27] O. Gul, D. J. van Woerkom, I. van Weperen, D. Car, S. R. Plissard, E. P. A. M. Bakkers, and L. P. Kouwenhoven, *Nanotechnology* **26**, 215202 (2015).
- [28] A. C. Ford, J. C. Ho, Y.-L. Chueh, Y.-C. Tseng, Z. Fan, J. Guo, J. Bokor, and A. Javey, *Nano Lett.* **9**, 360 (2009).
- [29] K.-F. Berggren and D. Newson, *Semicond. Sci. Technol.* **1**, 327 (1986).
- [30] M. T. Björk, A. Fuhrer, A. E. Hansen, M. W. Larsson, L. E. Fröberg, and L. Samuelson, *Phys. Rev. B* **72**, 201307 (2005).
- [31] C. W. J. Beenakker and H. van Houten, *Solid State Phys.* **44**, 1 (1991).
- [32] C. W. J. Beenakker, H. van Houten, and B. J. van Wees, *Superlattices Microstruct.* **5**, 127 (1989).
- [33] F. Vigneau, O. Gül, Y.-M. Niquet, D. Car, S. R. Plissard, W. Escoffier, E. P. A. M. Bakkers, I. Duchemin, B. Raquet, and M. Goiran, *Phys. Rev. B* **94**, 235303 (2016).
- [34] Y. M. Niquet, A. Lherbier, N. H. Quang, M. V. Fernández-Serra, X. Blase, and C. Delerue, *Phys. Rev. B* **73**, 165319 (2006).
- [35] J.-M. Jancu, R. Scholz, F. Beltram, and F. Bassani, *Phys. Rev. B* **57**, 6493 (1998).
- [36] T. Richter, C. Blömers, H. Lüth, R. Calarco, M. Indlekofer, M. Marso, and T. Schäpers, *Nano Lett.* **8**, 2834 (2008).
- [37] O. Gül, N. Demarina, C. Blömers, T. Rieger, H. Lüth, M. I. Lepsa, D. Grützmacher, and T. Schäpers, *Phys. Rev. B* **89**, 045417 (2014).
- [38] M. Royo, C. Segarra, A. Bertoni, G. Goldoni, and J. Planelles, *Phys. Rev. B* **91**, 115440 (2015).